A material view on extrinsic magnetic domain wall pinning in cylindrical CoNi nanowires

Michael Schöbitz, Ondrej Novotný, Beatrix Trapp, Sebastian Bochmann, Laurent Cagnon, Christophe Thirion, Aurélien Masseboeuf, Eric Mossang, Olivier Fruchart, Julien Bachmann

▶ **To cite this version:**

Michael Schöbitz, Ondrej Novotný, Beatrix Trapp, Sebastian Bochmann, Laurent Cagnon, et al.. A material view on extrinsic magnetic domain wall pinning in cylindrical CoNi nanowires. Journal of Physical Chemistry C, 2023, 127 (5), pp.2387-2397. 10.1021/acs.jpcc.2c07687 . hal-03468203

HAL Id: hal-03468203
https://hal.science/hal-03468203v1

Submitted on 9 Feb 2023

HAL is a multi-disciplinary open access archive for the deposit and dissemination of scientific research documents, whether they are published or not. The documents may come from teaching and research institutions in France or abroad, or from public or private research centers.

L'archive ouverte pluridisciplinaire **HAL**, est destinée au dépôt et à la diffusion de documents scientifiques de niveau recherche, publiés ou non, émanant des établissements d'enseignement et de recherche français ou étrangers, des laboratoires publics ou privés.

Distributed under a Creative Commons Attribution 4.0 International License

A material view on extrinsic magnetic domain wall pinning in cylindrical CoNi nanowires

M. Schöbitz,[*,†,‡,¶] O. Novotný,[†] B. Trapp,[¶] S. Bochmann,[‡] L. Cagnon,[¶] C. Thirion,[¶] A. Masseboeuf,[†] E. Mossang,[¶] O. Fruchart,[†] and J. Bachmann[*,‡,§]

†*Univ. Grenoble Alpes, CNRS, CEA, Spintec, Grenoble, France*

‡*Friedrich-Alexander Univ. Erlangen-Nürnberg, Chemistry of Thin Film Materials, Erlangen, Germany*

¶*Univ. Grenoble Alpes, CNRS, Institut Néel, Grenoble, France*

§*Technical University of Denmark, National Center for Nano Fabrication and Characterization, Kongens Lyngby, Denmark*

E-mail: michael.schobitz@gmail.com; julien.bachmann@fau.de

Abstract

Speed and reliability of magnetic domain wall (DW) motion are key parameters that must be controlled to realize the full potential of DW-based magnetic devices for logic and memory applications. A major hindrance to this is extrinsic DW pinning at specific sites related to shape and material defects, which may be present even if the sample synthesis is well controlled. Understanding the origin of DW pinning and reducing it is especially desirable in electrochemically deposited cylindrical magnetic nanowires (NWs), for which measurements of the fascinating physics predicted by theoretical computation have been inhibited by significant pinning. We experimentally investigate DW pinning in Co_xNi_{100-x} NWs, by applying quasistatic magnetic fields. Wire compositions were varied with $x = 20, 30, 40$, while the microstructure was changed by annealing or by varying the pH of the electrolyte for deposition. We conclude that pinning due to grain boundaries is the dominant mechanism, decreasing

inversely with both the spontaneous magnetization and grain size. Second-order effects include inhomogeneities in lattice strain and the residual magnetocrystalline anisotropy. Surface roughness, dislocations and impurities are not expected to play a significant role in DW pinning in these wire samples.

Introduction

The motion of domain walls (DWs) has been a point of high interest in magnetism since the early 20$^{\text{th}}$ century,[1] as it is often involved in magnetization reversal processes. Extensive efforts have been made to comprehend the underlying physics and its link with sample shape and microstructure. One-dimensional nanosized conduits such as strips and wires are a textbook case to model and therefore understand DW motion, owing to the small number of degrees of freedom involved.[2–5] The rise of spintronics brought prospects for a wide range of applications for DW motion in such conduits. Some prime examples include the dynamic switching of magnetic tunnel junctions or spin valves,[6] the ultra-fast speeds achieved in compensated ferrimagnets[7] or the progress made towards realizing a non-volatile shift-register memory device.[8–10] Across all of these, reliability and wall velocity stand out as critical parameters governing viability. While the physics of DW motion is now rather well understood, both reliability and velocity may suffer from imperfections in material and shape, called extrinsic pinning sites.[11–15] These act as energy wells or barriers that a DW must overcome[16,17] to move, translating into a minimum driving force that must be applied to allow for wall motion past each pinning site, such as a critical depinning field, H_{dep}, or critical depinning current, j_{dep}, for the case of DW motion induced by the application of an external magnetic field or spin-transfer torque, respectively.

The detailed nature of extrinsic pinning sites is unclear even in simple one-dimensional magnetic systems. Various ideas have been put forth, including compositional changes along the sample length,[18–20] polycrystallinity and associated grain boundaries,[14,21] surface defects and roughness,[11,13] dislocations,[22] impurities[23] or strain,[24,25] which all lead to local variations in magnetic properties such as magnetocrystalline anisotropy, spontaneous magnetization, exchange stiffness, etc and therefore variations in the energy landscape felt by the DW.

Among one-dimensional magnetic conduits, there exists a specific interest in cylindrical ferromagnetic

nanowires (NWs), synthesized by electrochemical deposition into porous membranes.[26] In such NWs with length $\gg$ diameter, DWs may be of either the transverse-vortex, or the Bloch-point type.[3,27] Theory and simulations predict fascinating novel physics in these 3D systems,[28] such as DW velocities in excess of $1\,\mathrm{km/s}$ with no Walker breakdown,[3,29] only limited by the emission of spin waves (spin-Cherenkov effect).[30,31] We recently provided a first experimental evidence of the very high velocities[15] in CoNi NWs, however, the results were affected by DW pinning, resulting in a large spread in the results. The pinning field in cylindrical NWs is typically one order of magnitude higher than in thin flat strips of the same material however deposited by physical methods.[32] This obstacle must be overcome in order to further study the fascinating fast motion of DWs and associated effects in these systems.

A vast quantity of reports concern the coercivity of NWs.[33–41] In most cases, especially for rather soft-magnetic materials, this relates to the nucleation of DWs from a wire end, shown to depend only on the geometry and materials parameters. For instance, coercivity in $\mathrm{Co}_x\mathrm{Ni}_{100-x}$ NWs shows a minimum of nucleation field for composition $x = 40$.[26,40] However, the nucleation field in such NWs is larger than H_{dep}, so that the DW runs the entirety of the wire once nucleated, and nothing is learned about extrinsic pinning through coercivity. Far fewer studies have focused on pinning. These largely theoretical and simulation-based works have considered DW pinning on diameter[42–46] or composition modulations,[19,20,47] on surface roughness[13,42] and on regions with different magnetocrystalline anisotropy, which can be likened to a polycrystalline texture.[13,48] All successfully identify that these material defects cause DW pinning, and some relate them primarily to variations in magnetostatic and anisotropy energy. However, only Ivanov and Orlov[13] provide a detailed theoretical picture of DW pinning due to surface roughness and polycrystallinity. A limited number of experimental pieces of work have focussed on pinning sites fabricated on purpose, through composition[20] or diameter modulations.[43,44] Other possible explanations for DW pinning, such as grain boundary pinning, have not been supported experimentally.

In this paper, we address the issue of DW pinning in cylindrical NWs with rather soft-magnetic properties, by evaluating experimentally the impact of various types of defects on DW pinning in $\mathrm{Co}_x\mathrm{Ni}_{100-x}$ NWs. By focusing on NWs with length $\gg$ diameter, we may disregard effects of magnetostatics arising from the wire ends. Also, considering individual NWs, we eliminate collective effects arising from neighboring NWs, such as is the case for the arrays inside porous templates.[41] We consider compositions in the

range of 20 to 40 % Co with a view to exhibit a low-pinning material, since we may expect low pinning from $Co_{40}Ni_{60}$ NWs that exhibit the lowest coercive field,[26] or from $Co_{20}Ni_{80}$ material that exhibits near-zero magnetocrystalline anisotropy and magnetostriction.[49] We compare quantitative experimental data with the trends expected from various potential physical causes of DW pinning based on the models proposed in the literature. Individual models being always reliant on some assumptions or simplifications, we consider several models where applicable, and we rely on the scaling laws predicted for each DW pinning mechanism for interpretation, rather than on the absolute numbers calculated from a particular model. Scaling laws being more general individual models, they allow us to draw more robust conclusions.

Methods

For the electrochemical deposition of NWs, templates of porous anodized aluminium oxide (AAO) membranes were synthesized as described elsewhere[26] and a coating of Au was sputtered on a single side to provide an electric contact for electrodeposition. We fabricated samples with compositions $Co_{20}Ni_{80}$, $Co_{30}Ni_{70}$ and $Co_{40}Ni_{60}$ starting from modified Watt's electrolytes with compositions summarized in Table 1. The electrolyte pH was set to 2.5 for all depositions, except once lowered to 1.5 to reduce the NW grain size with respect to the standard sample,[50,51] by adding NaOH or H_2SO_4. Depositions were carried out in a three-electrode electrochemical cell at $-1.1\,\mathrm{V}$ *vs.* an Ag/AgCl/NaCl (3 M) reference electrode. NW growth rates were controlled so as to grow wires of lengths 30 to 35 µm in all cases, except for the deposition with an electrolyte pH of 1.5 for which NW lengths were only 12 to 15 µm. After NW growth, the gold contact was etched in a KI/I_2 solution. Annealing of some batched was carried out to allow for grain growth and crystallographic relaxations,[52–54] by placing filled membranes into a tubular vacuum oven at 500 °C for 20 min.

NW compositions were checked by atomic absorption spectroscopy (AAS) and by scanning electron microscopy energy-dispersive X-ray (SEM EDX) analysis. Vibrating sample magnetometry (VSM) and X-ray diffraction (XRD) were carried out on large ($2 \times 2\,\mathrm{mm}^2$) pieces of filled AAO membrane. For XRD, diffractograms were obtained with a symmetric $\theta - 2\theta$ geometry and a Cu K_α X-ray source (1.5402 Å wavelength). Individual diffraction peaks in a diffractogram were fitted using a Gaussian to extract both

Table 1: Composition of various electrolytes and mass per $100\,\mathrm{mL}$ used to electrochemically grow NWs with a given composition. Low pH depositions used the same electrolyte composition, resulting in slower growth rates but similar NW compositions. The solid composition was determined by atomic absorption spectroscopy, see the Methods section and Fig. S2 in the supporting information for further details. The homogeneity of composition along the length of the wires is demonstrated by X-ray microanalysis profiles (Fig. S3).

	$Co_{20}Ni_{80}$		$Co_{30}Ni_{70}$		$Co_{40}Ni_{60}$	
Compound	n (mol)	m (g)	n (mol)	m (g)	n (mol)	m (g)
$CoSO_4{\cdot}7H_2O$	0.0182	0.5104	0.0282	0.7930	0.0450	1.2649
$CoCl_2{\cdot}6H_2O$	0.0012	0.0276	0.0018	0.0428	0.0027	0.0649
$NiSO_4{\cdot}6H_2O$	0.3120	8.2005	0.2934	7.7109	0.2375	6.2426
$NiCl_2{\cdot}6H_2O$	0.0551	1.3087	0.0518	1.2306	0.0400	0.9508
H_3BO_3	0.5000	3.0915	0.5000	3.0915	0.5000	3.0915
saccharin	0.0150	0.2750	0.0150	0.2750	0.0150	0.2750

peak position and peak width.

NWs were freed from the AAO template by dissolving alumina in either $0.6\,\mathrm{M}$ chromic and $0.4\,\mathrm{M}$ orthophosphoric acid solution at $70\,^{\circ}\mathrm{C}$ for 3 hours, or in $2\,\mathrm{M}$ NaOH at $60\,^{\circ}\mathrm{C}$ for 2 hours. The latter method was only used where specifically noted in the text. The resulting suspensions were then subjected to several rounds of centrifugation and rinsing in distilled water and finally in ethanol to produce clean NW suspensions. Drops of suspension were then dispersed onto silicon wafers with prepared gold alignment marks and NWs were located using SEM. These marks allowed to seek the wires using only the optical view of the magnetic force microscope (MFM), which was used to monitor DW motion. Individual NW samples were also imaged with transmission electron microscopy (TEM), by dispersing NWs on a specific lacey-carbon grid.

Basic magnetic characterization of the wires by magnetometry of full samples of wires still embedded in the matrix exhibit the expected anisotropy and values of the spontaneous magnetization M_S, in agreement with values calculated from the composition (Fig. S4 and Table S1 in the Supporting Information). DWs were nucleated along the NW by means of a decaying oscillating external magnetic field with maximum strength $2\,\mathrm{T}$, applied perpendicular to the wire long axis (perpendicular to the plane of the Si wafer substrate).

Results

DW depinning was measured by imaging DW positions with MFM before and after applying an external magnetic field oriented along the NW long axis, with pulse duration of about $1\,\mathrm{s}$. By slightly increasing the amplitude of the applied field between each measurement, the field required to depin DWs from specific pinning sites could be determined. Fig. 1a shows an atomic force microscopy (AFM) image of a section of an individual, as-deposited $90\,\mathrm{nm}$-diameter $Co_{30}Ni_{70}$ NW. The corresponding MFM image in Fig. 1b shows the initial magnetic configuration with two DWs located along the wire length, and the direction of magnetization within the three longitudinal domains indicated by green arrows.

The contrast in MFM largely reflects the stray magnetic field arising from the sample. In our case, the magnetic contrast surrounding the observed DWs reflects the magnetic flux arising from a DW in a NW. Although transverse-vortex and Bloch-point type DWs have different distributions of magnetization and thus of magnetic charges, either of volume or surface type, the total amount of charge is the same in both situations. It is set by topology to $2SM_\mathrm{s}$, with S the cross-sectional area of the wire and M_s the spontaneous magnetization of the material.[55] Thus, the total magnetic flux arising from the two types of DWs is the same, and in practice the two can hardly be differentiated with MFM. Besides, for a NW diameter larger than typically seven times the dipolar exchange length, *i.e.*, from 25 to $50\,\mathrm{nm}$ from Co-rich to Ni-rich alloys,[56] the Bloch-point wall is that of lowest energy. However, the energy difference with the transverse-vortex wall is minute and in practice both DWs are found in such cylindrical NWs.[57,58] Finally, during motion driven by application of magnetic field, the DW type may change from one to the other type.[59] Therefore, in the present work we cannot discriminate the importance of the DW type on pinning.

The MFM image in Fig. 1c shows the magnetic configuration after applying a magnetic field pulse with amplitude $-12\,\mathrm{mT}$, remaining unchanged. Imaging after applying a $-13\,\mathrm{mT}$ field pulse (Fig. 1d) shows that the left-hand wall was depinned and moved to a different, presumably stronger pinning site, hence the depinning field of the initial site is in the range $12\,\mathrm{mT}$ to $13\,\mathrm{mT}$. Such measurement series were repeated on multiple NWs for each sample type in order to determine a distribution of depinning field amplitudes.

Fig. 1e,f shows the distribution of depinning field for both as-deposited and annealed $Co_{30}Ni_{70}$ NWs, respectively. Note that the procedure of applying quasistatic pulses of field with rising values during a series implies that for any given wire contributing to the statistics in these figures, once the first depinning

event has occurred we cannot measure events associated with lower pinning fields. Thus, these distributions probably over-emphasize pinning sites associated with a high value of field, partly contributing to their large width. Still, the average and standard deviation of the distributions are plotted as horizontal error-bars, illustrating a lower average depinning field of the as-deposited sample. The variation of average depinning field as a function of cobalt content and different preparation methods is presented in Fig. 1g, with different NW diameters indicated by marker shapes. In the case of the as-deposited NW samples (blue), the average depinning field decreases from 18 ± 4 to 13 ± 4 to $7 \pm 2\,\mathrm{mT}$ as the Co content increases from 20 to 30 to 40 %. This nearly linear decrease is indicated by the dashed guide to the eye. NWs deposited from an electrolyte with a pH of 1.5 (Fig. 1g, green) exhibit a lower average depinning field compared to the NWs deposited from a normal electrolyte with a pH of 2.5 (blue). Conversely, NWs that were annealed in the AAO membrane at $500\,^{\circ}\mathrm{C}$ for $20\,\mathrm{min}$ (Fig. 1g, red) display a larger average depinning field (data from Fig. 1f).

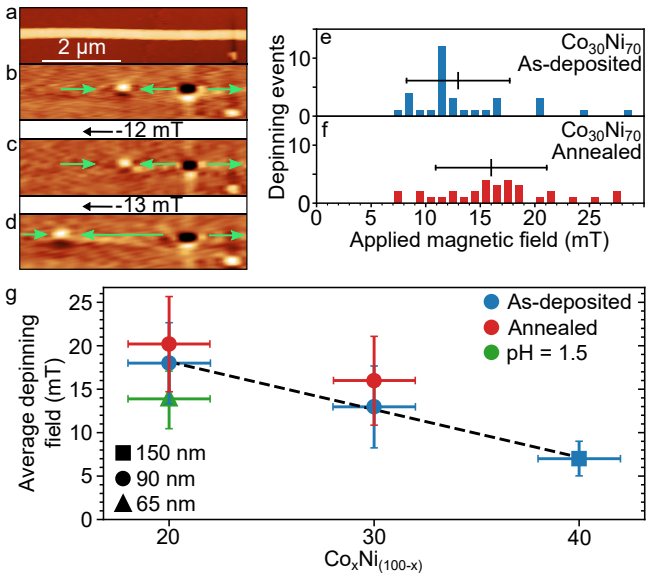

Fig. 1: DW depinning in NWs. (a) AFM image of a section of an as-deposited $90\,\mathrm{nm}$-diameter $Co_{30}Ni_{70}$ NW, with the initial magnetic configuration of the same section shown in the MFM image in (b). There are two DWs present and the magnetization of the longitudinal domains is indicated by green arrows. (c, d) MFM images taken after the application of -12 and $-13\,\mathrm{mT}$ fields in the indicated direction, respectively, showing the depinning and subsequent pinning of the left hand DW at $-13\,\mathrm{mT}$. (e, f) Distributions of depinning fields for $Co_{30}Ni_{70}$ as-deposited and annealed NWs, respectively, with the average value and standard deviation indicated by the horizontal lines. (g) Average depinning field as a function of NW cobalt content, for as-deposited NWs (blue), annealed NWs (red) and as-deposited NWs deposited with an electrolyte pH $= 1.5$ (green). NW diameters vary from $150\,\mathrm{nm}$ (squares) to $90\,\mathrm{nm}$ (circles) to $65\,\mathrm{nm}$ (triangles) and the dashed line acts as a guide to the eye.

It is evident from Fig. 1g that NW samples prepared by different methods lead to variations in average depinning fields. To tentatively separate the effects of composition and microstructure between the samples, we used XRD to analyze the various NWs while in the AAO membranes. The XRD diffractogram of as-deposited $Co_{20}Ni_{80}$ NWs is shown in blue in Fig. 2a. The peaks at $2\theta = 44.51, 51.78, 76.35, 92.92°$ are consistent with reflections from the (111), (200), (220), and (311) planes of face-centered cubic CoNi alloy, while the peaks at 64.6, 77.7 and $82.6°$ are consistent with diffraction from gold, suggesting that the etching of the bottom electrode is incomplete. The absence of any other peak indicates the single phase of the electrodeposited NWs.

After subtraction of the calibrated instrumental angular offset, the diffraction peak angles were used to calculate the lattice coefficient a, of the sample's cubic unit cell, according to Bragg's law, giving an average $\langle a \rangle = 3.525 \pm 0.001$ Å (Fig. 2b). This is slightly below the expected value of the lattice coefficient for $Co_{20}Ni_{80}$, $a_{\mathrm{th}} = 3.5279$ Å, calculated using Vegard's law, indicating a general compression of the unit cell with respect to the equilibrium state, at least along the wire axis. This corresponds to an average crystal strain $\langle \epsilon \rangle = -8.2 \times 10^{-4} \pm 1.7 \times 10^{-4}$. Annealing of the $Co_{20}Ni_{80}$ NWs sample does not change the XRD pattern (Fig. 2a, red) qualitatively, however, a similar calculation of the lattice coefficient gives $\langle a \rangle = 3.526 \pm 0.002$ Å and thus possibly an increase in unit cell size, although affected by the error bar. At this stage we need to discuss the impact of the AAO membrane. Heating of the AAO and its concomitant thermal expansion leads to a reduction of the pore diameter. This and the NW's own thermal expansion cause a radial stress of the wire, which would tend to cause an expansion along the wire axis. This is reversed upon cooling, however, the original shape may not be entirely recovered, leaving a difference with the non-annealed sample. Further, as the sample is quickly removed from the oven, the rapid cooling that occurs could be linked to quenching and partly freeze the expanded high-temperature structure.[22]

Fig. 2b shows the lattice coefficients calculated from XRD peak positions of all samples, with horizontal dashed lines indicating a_{th} for the given composition.[53] For both the as-deposited (blue) and the annealed samples (red), $\langle a \rangle$ increases with increasing Co content, as expected from the larger lattice parameter of Co than of Ni, and from Vegard's law. All as-deposited samples, except the previously-discussed $Co_{20}Ni_{80}$, have an excellent match between $\langle a \rangle$ and a_{th}, and it thus follows that the crystallites within the electrodeposited material are essentially free of average crystal strain. Furthermore, annealing leads to an increase in $\langle a \rangle$,

however, unlike the previously discussed case of annealed $Co_{20}Ni_{80}$, the other three instances of annealing ($Co_{20}Ni_{80}$ with pH $= 1.5$, $Co_{30}Ni_{70}$ and $Co_{40}Ni_{60}$) lead to $\langle a \rangle > a_{\mathrm{th}}$, indicative of crystal lattices under slight tensile stress along the NW axis and therefore a slight positive average crystal strain8 $\langle \epsilon \rangle$. Finally, $Co_{20}Ni_{80}$ NWs electrodeposited from an electrolyte with a pH of 1.5 exhibit a larger lattice coefficient than standard growth $Co_{20}Ni_{80}$ NWs, and in the end closer to a_{th}. This may be the result of the significantly slower deposition rate, allowing atoms to rearrange and grow overall less strained crystals. A summary of the different crystal strain of each sample is displayed in Table 2.

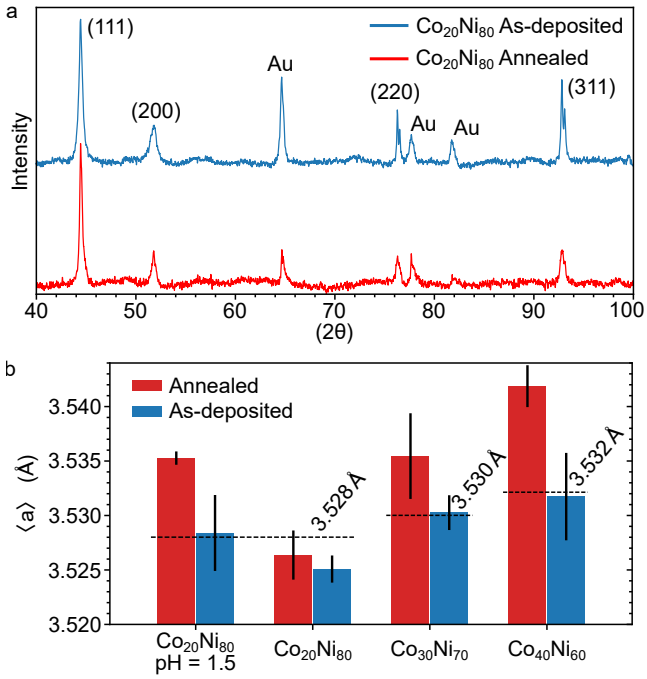

Fig. 2: XRD analysis of NW crystallography. a) Individually rescaled XRD diffractograms of $Co_{20}Ni_{80}$ NWs enclosed in an AAO membrane pre (blue) and post (red) annealing at $500\,^{\circ}\mathrm{C}$ for $20\,\mathrm{min}$. The peaks corresponding to face-centered cubic CoNi are indexed, while the remaining peaks at 64.6, 77.7 and $82.6°$ result from the remainder of the gold bottom electrode. Fig. S5 in the Supporting Information provides direct comparisons between several samples, zooming in on the (111) and (200) peaks. b) Average lattice coefficients, $\langle a \rangle$, in Å, calculated from XRD peak positions for all samples, pre (blue) and post (red) annealing. Theoretical lattice parameters calculated with Vegard's law for the given composition are indicated by the dashed lines.

Further microstructural information can be obtained using the Williamson-Hall approach,[60,61] to separate the effects of amplitude of distribution of crystal strain $\Delta\epsilon$, and grain size D, on peak broadening β, of the XRD diffractogram. $\Delta\epsilon$, also called inhomogeneous strain, reflects the spatial distribution of lattice parameters around a mean value $\langle \epsilon \rangle$, in different grains or within grains. This method is more suitable

than relying on the simple Scherrer formula, which can underestimate the grain size, affected by $\Delta\epsilon$ and instrumental resolution. Indeed, both $\Delta\epsilon$ and D contribute to the finite width of peaks, the first contributing to a spread of every diffraction peak and depending on the angle 2θ, the second contributing to a given peak width independent of the angle, scaling as $1/D$ (Scherrer formula). In other words, the impact of a non-zero $\Delta\epsilon$ increases at large 2θ, whereas the effect of D remains constant. Therefore, after correcting for instrumental peak broadening in the XRD diffractogram, the impact of $\Delta\epsilon$ and D can be separately identified by monitoring $\beta\cos\theta = 4\Delta\epsilon\sin\theta + k\lambda/D$ versus $\sin(\theta)$, with λ the X-ray wavelength and k a shape factor best approximated as 0.9. A Williamson-Hall plot for as-deposited $Co_{20}Ni_{80}$ with pH $= 1.5$ NWs is shown in Fig. 3a. From the above equation, the slope ($4\Delta\epsilon$) and y-intercept ($k\lambda/D$) of the blue linear regression of the data set provide the amplitude of strain distribution and grain size, respectively. Besides the fitting error, the error for this information should take into consideration the maximum and minimum possible slopes, as shown by dashed lines, however, with the minimum slope not below zero since $\Delta\epsilon < 0$ is unphysical. The full Williamson-Hall plot for both as-deposited and annealed NWs is given in Fig. 3b, showing the linear regression fits of as-deposited and annealed samples as solid and dashed lines, respectively. For the as-deposited $Co_{20}Ni_{80}$ and $Co_{30}Ni_{70}$ NW data the regression slope should be negative from the numerical fit, albeit bounded to zero slope as a constraint associated with its physical meaning, as mentioned above.

Fig. 3c shows the average grain size, its associated error bar, and the distribution of strain, for both as-deposited (full bar) and annealed (open bar) NWs, calculated from the Williamson-Hall plot. The error bars are calculated by the same method using the maximum and minimum possible fitted lines, however, note that the error bars for annealed $Co_{20}Ni_{80}$ with pH $= 1.5$ and $Co_{30}Ni_{70}$ extend to $> 1\,\mu\mathrm{m}$, which exceeds the instrumental limit for peak widths below $0.02°$ in 2θ and thus $D_{\max} \lesssim 400\,\mathrm{nm}$. Grain sizes calculated using the Scherrer formula, $D = k\lambda/(\beta\cos\theta)$, again with the shape factor $k = 0.9$, should provide a lower bound for grain size, as discussed previously. These are indicated by grey crosses, which match indeed well the lower bound of the error bars. The grain size of standard as-deposited NWs is $\approx 20\,\mathrm{nm}$, with little change in composition. However, it must be noted that the large data spread and uncertainties in the Williamson-Hall plot may affect the accuracy of these calculated values. Decreasing the electrolyte pH reduces the grain size to $15\,\mathrm{nm}$ ($Co_{20}Ni_{80}$ with pH $= 1.5$), possibly resulting from the increased hydrogen evolution at the cathode. This inhibits grain growth by limiting surface diffusion of adatoms and instead favors grain nucleation.[62]

Table 2: Summary of XRD structural information, showing average lattice coefficient a, as well as the average lattice strain $\langle\epsilon\rangle$, and the associated uncertainty arising from instrumental precision, and fitting of peak positions in the XRD diffractogram. Furthermore, values from the Williamson-Hall analysis for the amplitude of distribution of inhomogeneous crystal strain $\Delta\epsilon$ are given, together with the respective minimum and maximum for this strain distribution which are a result of the uncertainty in the linear fit for the Williamson-Hall analysis.

NW composition	Sample	$\langle a\rangle$ (Å)	$\langle\epsilon\rangle$ (10^{-4})	$\langle\epsilon\rangle$ uncertainty (10^{-4})	$\Delta\epsilon$ (10^{-4})	$\Delta\epsilon_{\min}$ (10^{-4})	$\Delta\epsilon_{\max}$ (10^{-4})
$Co_{20}Ni_{80}$ pH= 1.5	As-deposited	3.528	1.1	±6.4	7.4	0	28.1
	Annealed	3.535	18.8	±9.8	11.7	1.1	24.6
$Co_{20}Ni_{80}$	As-deposited	3.525	−8.2	±1.7	0	0	3.5
	Annealed	3.526	−4.6	±5.7	6.7	0	18.1
$Co_{30}Ni_{70}$	As-deposited	3.530	0.4	±4.5	0	0	27.0
	Annealed	3.535	15.0	±11.1	18.8	0	38.6
$Co_{40}Ni_{60}$	As-deposited	3.532	−1.3	±5.2	-	-	-
	Annealed	3.542	27.3	±5.4	-	-	-

Conversely, annealing clearly increases the grain size to 35 , 55 and $114\,\mathrm{nm}$ for $Co_{20}Ni_{80}$, $Co_{20}Ni_{80}$ with pH $= 1.5$ and $Co_{30}Ni_{70}$, respectively, as expected from recrystallization and growth initiated by the heat treatment.[52–54] Similarly, the amplitude of inhomogeneous crystal strain was calculated from the slope as $4\Delta\epsilon$. Where the linear regression slope was positive, the strain distribution $\Delta\epsilon$ was calculated as 6.7×10^{-4} (annealed $Co_{20}Ni_{80}$), 7.4×10^{-4} ($Co_{20}Ni_{80}$ with pH $= 1.5$), 1.17×10^{-3} (annealed $Co_{20}Ni_{80}$ with pH $= 1.5$) and 1.18×10^{-3} (annealed $Co_{30}Ni_{70}$), however, for some measurements the uncertainty for this calculation extends to nearly one order of magnitude larger values. $\Delta\epsilon$ as well as the maximum and minimum possible values for $\Delta\epsilon$ are also displayed in Table 2. All in all, the distribution of strain is in the range 1×10^{-3} to 3×10^{-3}, with the larger values found in annealed samples.

The grain sizes and strain distributions that we measure are very similar to values for nanocrystalline nickel thin films, also electrodeposited from a Watt's or purely sulfate electrolyte. A large number of studies made use of the Scherrer formula and found grain sizes of the order of 10 to $50\,\mathrm{nm}$, for deposition conditions close to the ones used in this work.[63–67] Fewer studies have investigated electrodeposited NiCo alloys,[53,68] but the reported grain sizes largely match those of pure Ni. In particular, Tóth *et al.*[53] investigated the effect

of annealing at $300\,^{\circ}\mathrm{C}$ for $1\,\mathrm{h}$ on the grain size of nanocrystalline CoNi alloys and found an increase from 10 to $40\,\mathrm{nm}$ for low Co contents. The experiment that is most similar to the present study was performed by Dost *et al.*,[69] where annealing of $275\,\mathrm{nm}$-diameter Ni NWs at $650\,^{\circ}\mathrm{C}$ for $1\,\mathrm{h}$ increased the grain size from 8 to $160\,\mathrm{nm}$. TEM imaging also revealed that after annealing grains often occupied the entire diameter of the wire. The grain sizes of our as-deposited materials match well with values from literature, however, a direct comparison of the impact of annealing in this study and previous literature cannot be made, because the starting material and annealing recipes differ. Regarding the grain size of deposits made with a lower electrolyte pH, there are no reports on nanocrystalline CoNi and other studies investigate pH > 2. Still, in the CoFe alloys studied by Riemer *et al.*,[62] a 50 to $30\,\mathrm{nm}$ grain size reduction was reported when changing the pH from 3 to 2 and in the NiCu alloys studied by Alper *et al.*[51] a 120 to $90\,\mathrm{nm}$ grain size reduction was reported when changing the pH from 3.3 to 2. Strain distribution is considered less often than grain size, especially since most studies discuss only the Scherrer formula to analyse XRD peak broadening. The studies that do report on strain distribution in nanocrystalline Ni films find $\Delta\epsilon \lesssim 0.005$[54,67] and Wang *et al.*[54] note that this reduces by $30\,\%$ by annealing at $100\,^{\circ}\mathrm{C}$ for $1\,\mathrm{h}$.

Discussion of the origin of pinning

DW pinning should not occur in a homogeneous singlecrystalline NW with a perfect cylindrical shape. However, such a wire is unachievable in practice, and any deviation from perfection should lead to DW pinning. This includes diameter modulation and surface roughness, polycrystallinity and the associated grain boundaries, strain, changes in composition, line and point defects such as dislocations and impurities. Based on the results presented in the previous section, we evaluate below the phenomena most likely responsible for DW pinning, grouping them in three categories: i) surface roughness and other shape defects; ii) polycrystallinity and its interplay with magnetocrystalline anisotropy and inverse magnetostriction; iii) material defects such as inhomogeneities, grain boundaries, dislocations, impurities. General aspects applying to those different situations are described first, in the paragraph below.

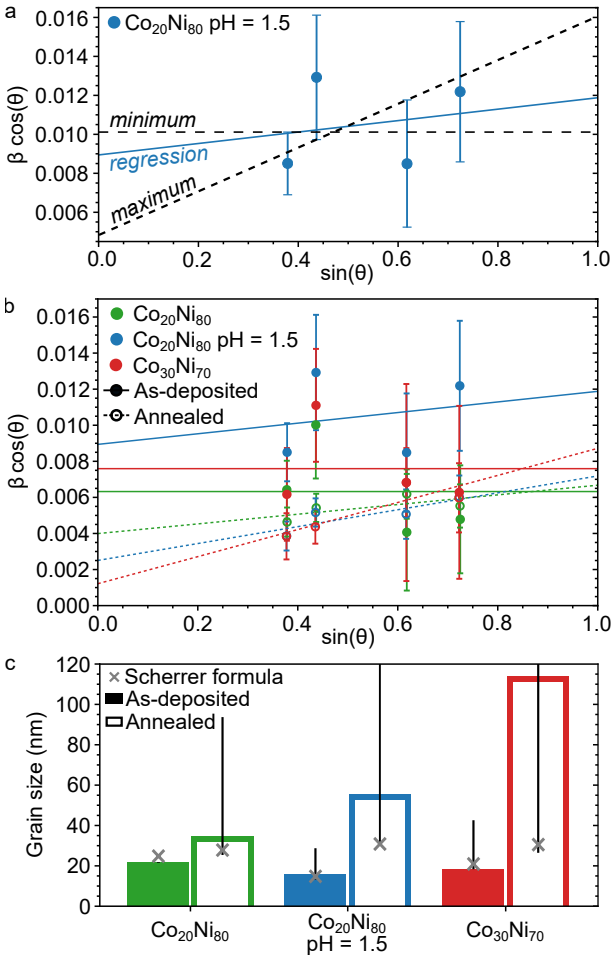

Fig. 3: Williamson-Hall analysis of different NW samples. a) Williamson-Hall plot for as-deposited $Co_{20}Ni_{80}$ with pH $= 1.5$ NWs. The linear regression fit (blue line) and maximum and minimum possible slopes which provide the error (black dashed lines), are indicated. b) The same Williamson-Hall plot for as-deposited (full circles) and annealed (open circles) $Co_{20}Ni_{80}$ (green), $Co_{20}Ni_{80}$ with pH $= 1.5$ (blue) and $Co_{30}Ni_{70}$ (red) NWs. Linear regression fits are shown as solid and dashed lines for as-deposited and annealed samples, respectively, the y-intercept of which are inversely proportional to the grain size of the sample. c) Grain size (nm) as calculated by the Williamson-Hall method for as-deposited (solid bar) or annealed (open bar) NW samples. Solutions from the Scherrer formula are indicated by grey crosses. Note that the error bars of the annealed $Co_{20}Ni_{80}$ with pH $= 1.5$ and annealed $Co_{30}Ni_{70}$ extend to over $1\,\mu m$ and therefore much past the limit of the instrumental precision.

General considerations

To set orders of magnitude, the models discussed are applied to a wall of length $\delta_W \simeq 2R$, a reasonable scaling law for the wire diameters considered here, in the range a few tens to a hundred of nanometers.[56] We will also use the textbook model of Becker-Kondorski[16,70] for DW pinning in a one-dimensional framework,

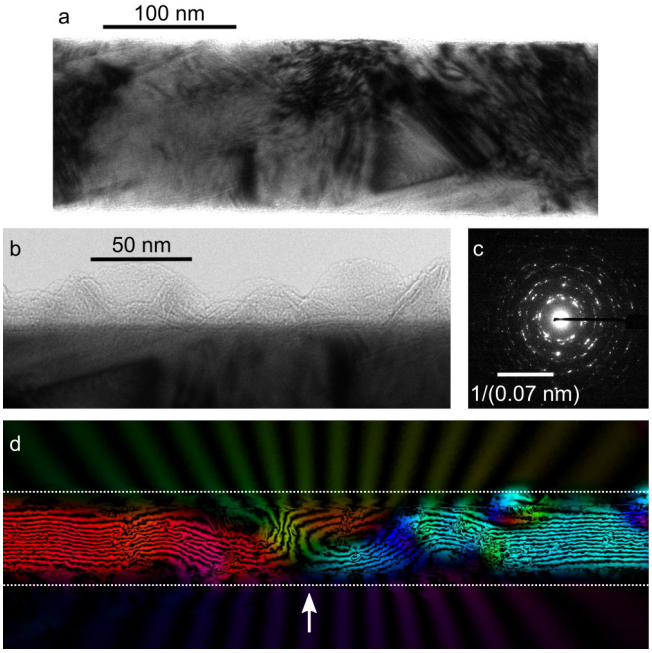

Fig. 4: TEM images of a $130\,\mathrm{nm}$-diameter $Co_{40}Ni_{60}$ NW freed from the AAO membrane by dissolution in NaOH solution to correlate DW pinning sites, surface roughness and microstructure. a,b) High resolution TEM images, showing in (a) the complex polycrystalline microstructure and in (b) a higher magnification on the edge of the same NW, revealing low surface roughness but strong oxide layer formation from dissolution in NaOH. Fig. S1 in the Supporting Information shows the original micrograph recorded for (a) together with the version presented here, in which brightness and contrast have been adjusted, and also shows the thinner native oxide layer resulting from dissolution in chromic and orthophosphoric acid solution instead. c) A diffraction pattern from the same type of $Co_{40}Ni_{60}$ NW. d) Electron holography image showing the magnetic flux reconstruction in- and outside the NW (outlined by white dotted lines), displayed as black lines superimposed on color map obtained from the electron phase gradient (color associated to in-plane direction). A DW (white arrow) is present at the same place observed with conventional imaging in (a).

relating the depinning field H_{dep} to the energy landscape $\mathcal{E}(x)$:

$$H_{\mathrm{dep}} = \frac{1}{2\mu_0 M_{\mathrm{s}} S} \frac{\mathrm{d}\mathcal{E}}{\mathrm{d}x}, \tag{1}$$

with M_{s} the spontaneous magnetization of the material, S the cross-sectional area of the one-dimensional conduit, πR^2 in the present situation, and $\mathcal{E}$ the position-dependent net energy of the DW, labeled in Joules.

Surface roughness

Here we evaluate to which extent deviations from perfect translational symmetry in the shape of a NW may explain the pinning of DWs in our systems. Deviation from the perfect cylindrical shape may take the form

of local modulations of diameter (*i.e.*, correlated around the wire diameter), or general roughness. Analytical modeling cannot cover the general case of pinning on such defects, and approximations must be made. To provide some generality and therefore robustness in the discussion and comparison with experiments, we consider three models of a very different kind.

A first model may be adapted from Bruno *et al.*, evaluating the contribution of dipolar energy to magnetic anisotropy in thin films, related to the existence of roughness.[71] This model predicts a cost for planar anisotropy amounting to a net energy, written

$$\mathcal{E}_{\mathrm{Bruno}} = \mathcal{S}\,\frac{1}{2}\mu_0 M_{\mathrm{s}}^2\,\frac{\sigma}{4}\left[1 - f\left(2\pi\frac{\sigma}{\xi}\right)\right]. \tag{2}$$

$\mathcal{S}$ is the surface area of the thin film considered, σ the average deviation for the roughness, ξ the correlation length. $f(0) = 1$ with an infinite negative slope, sharply decreasing to $f(0.1) \simeq 0.6$ and $f(1) < 0.1$. Assuming $(\sigma, \xi) \ll R$, one may neglect long-range correlations on magnetostatic energy, and therefore model the surface of a cylindrical wire with the rolled surface of a thin film. We combine Eq. (1) to Eq. (2) with $\mathcal{S} = 2\pi R\delta x$, considering a distance $\delta x = \xi$ equal to the roughness correlation length, and averaging azimuthally over a number of correlation areas $2\pi R/\xi$, we obtain a formula for the depinning field:

$$H_{\mathrm{Bruno}} = M_{\mathrm{s}}\,\frac{\sigma}{8R}\sqrt{\frac{\xi}{2\pi R}}\left[1 - f\left(2\pi\frac{\sigma}{\xi}\right)\right]. \tag{3}$$

A second model, proposed by Ivanov and Orlov, considers specifically the cylindrical geometry, with an azimuthally correlated roughness.[13] The models predicts that

$$H_{\mathrm{dep}} = 1.4\,M_{\mathrm{s}}\left(V_{\mathrm{d}}/\delta_{\mathrm{w}}^3\right)\sqrt{(\delta_{\mathrm{w}}/2R)\ln\left(L/\delta_{\mathrm{w}}\right)}. \tag{4}$$

$V_{\mathrm{d}} = 2\pi R\,\sigma\,\delta_{\mathrm{w}}$ is the volume of defects at the scale of a DW, and $\delta_{\mathrm{w}}^3 = 8R^3$. The $\ln\left(L/\delta_{\mathrm{w}}\right)$ term reflects the statistical distribution of strength of pinning sites on a long length scale L arising from fluctuations from defect to defect, while all other terms reflect a given defect. As Bruno's model considers a single defect, and in the experiments we also report one defect at a time, this term must be let aside, to discuss comparable

situation. Besides, we disregard the square root as $\delta_{\mathrm{w}} \simeq 2R$. We finally have:

$$H_{\mathrm{Ivanov}} = 1.4\, M_{\mathrm{s}}\, \frac{\pi}{2}\, \frac{\sigma}{R}\ . \tag{5}$$

Yet a third model, developed by Fernandez-Roldan *et al.*,[45] intends to describe gentle and controlled variations of diameter. The propagation field is close to $2M_{\mathrm{s}}(\mathrm{d}R/\mathrm{d}x)$. However, this model is valid for modulations larger than the wall width, which is opposite to the situation of roughness, so that we cannot simply consider that $\mathrm{d}R/\mathrm{d}x \approx \sigma/\xi$. Instead, as a rule of thumb we may renormalize the impact of the modulation of diameter with the length of the full DW, *i.e.*, with an extra coefficient $\xi/(2R)$. This leads to:

$$H_{\mathrm{FR}} = M_{\mathrm{s}} \frac{\sigma}{R}. \tag{6}$$

Interestingly, although all three models have a very different fundamental basis and a priori a distinct range of application, they all lead to pinning scaling with $M_{\mathrm{s}}\,\sigma/R$, simply with a different coefficient, and statistical azimuthal averaging for Bruno's model. This expectation is opposite to our experimental observation that the pinning field decreases with increasing M_{s} (Fig. 1). This suggests that roughness coupled with dipolar effects is not the leading mechanism of pinning in our case. This is consistent with the fact that wires electrochemically deposited in AAO templates are known to be very smooth, resulting from the amorphous structure of the aluminium oxide, unless modulations of diameter may result from instabilities during the anodization step.[72] TEM imaging of NWs similar to those studied here revealed that beyond a possible native oxide layer, no noticeable surface roughness could be observed (Fig. 4a,b, Fig. S1 in the Supporting Information). The material is polycrystalline (Fig. 4c). Further, imaging with TEM holography (Fig. 4d) showed that a DW was pinned along the low roughness wire segment shown already in 4a. Such low impact from pinning due to surface roughness may not be the case for polycarbonate templates, which display a roughness intrinsically linked with the molecular size of the underlying polymers.[57,73]

Polycrystallinity

Polycrystallinity may lead to spatial variations of the volume density of magnetic energy density K due to different grain orientations, and related to either magnetocrystalline anisotropy, or magnetoelastic anisotropy in the case of strained grains. Both convert into a position-dependent energy of a DW, which implies pinning. In magnetically soft bulk-like systems, this situation can be described with the Herzer model,[14,74] averaging the anisotropy energy over the large number of grains inside a DW. The width of the latter is found self-consistently to scale with $K^4 D^6/A^3$. This model is not suitable for cylindrical NWs, for which δ_W is largely determined by magnetostatics and possibly exchange, scaling approximately with $\approx 2R$ in our situation. Instead, we may consider the change of energy $\delta\mathcal{E}$ of a DW upon motion with distance $\delta x = D$, and apply the Becker-Kondorski model [Eq. (1)]. $\delta\mathcal{E} = K\sqrt{N}D^3$, with $N = 2\pi R^2/D^2$ the change of number of grains in the DW upon motion. This leads to:

$$H_\mathrm{poly} = \frac{1}{\sqrt{2\pi}} \frac{1}{\mu_0 M_\mathrm{s}} \frac{D}{R} K. \tag{7}$$

Let us apply Eq. (7) in the expected worst situation, *i.e.*, to our material with largest magnetocrystalline and magnetoelastic anisotropy $Co_{40}Ni_{60}$. At room temperature, the cubic coefficient for magnetocrystalline anisotropy is $K_1 \simeq 7\,\mathrm{kJ/m^3}$.[75] Concerning inverse magnetostriction, spatial fluctuations of magnetic anisotropy may result either from an average strain $\langle\epsilon\rangle$ and different crystalline orientations, or from spatial distribution of strain, related to $\Delta\epsilon$. Thus, we should consider the combination, or larger value of both, for a realistic approach, which is of the order of 3×10^{-3} (Table 2). The magnetoelastic coupling coefficients B_1 and B_2 are in the range of $10 \times 10^7\,\mathrm{J/m^3}$.[49] All in all, the resulting density of magnetic anisotropy may be $K_\mathrm{mel} \simeq 30\,\mathrm{kJ/m^3}$. Eq. (7) applied with $D = 20\,\mathrm{nm}$, $R = 50\,\mathrm{nm}$, $\mu_0 M_\mathrm{s} = 1.17\,\mathrm{T}$ and the above values for density of anisotropy energy leads to pinning fields $10\,\mathrm{mT}$ or below, which is similar to the experimental values. So, at first sight polycrystallinity could be a serious candidate to explain pinning. However, both magnetocrystalline anisotropy and magnetostriction are expected to vanish almost simultaneously for a composition around $Co_{20}Ni_{80}$, and be highest for $Co_{40}Ni_{60}$ in our range of composition, which would point at very weak pinning for the first, and maximum for the second. The experimental observations are opposite, which leads us to conclude that magnetocrystalline or magnetoelastic anisotropy energy in the grains of a

polycrystalline material are not the source of DW pinning in our NWs.

Material defects

A potential source of imperfections in the materials are inhomogeneities in composition of the CoNi alloy, leading to an axial gradient of magnetic energy for a DW. While this may be done on purpose[20] to engineer DW positions, undesired inhomogeneities may also arise from potential instabilities or limitations of diffusion during electroplating. However, SEM EDX line scans evidenced homogeneous compositions along the wire length in all of our studied samples (Fig. S3 in the Supporting Information). Besides, we would like to highlight that our detailed TEM and EDX investigations have provided no evidence for radial segregation within the Co/Ni alloy. Certainly, it is virtually impossible to prove the absence of any radial inhomogeneity from experimental data in a definitive manner.

A usual defect in materials is dislocations. Yu *et al.*[76] noticed that coercive fields increase for larger dislocation densities. Lindquist *et al.*[21] directly observed pinning on dislocations in bulk magnetite, in which higher dislocation densities and longer dislocation lengths increase depinning fields, while pinning is decreased for larger magnetization. This hints at an inhomogeneity of magnetoelastic anisotropy due to strain around the dislocation, balanced by the pressure induced on the DW by the Zeeman energy. The lowering of the micromagnetic energy around a dislocation has been modeled, promoting nucleation for magnetization reversal.[77] The increase of M_s and the experimental decrease of pinning for larger Co content are consistent, however, again we would expect very low pinning for the $Co_{20}Ni_{80}$ alloy with vanishing magnetostriction. Besides, it is known that annealing reduces dislocation lengths and densities[52–54] and thus pinning, while we observe an increase of pinning upon annealing (Fig. 1e-f). Therefore, dislocations are probably not the most active source of pinning in our case.

Another kind of material defect is grain boundaries. These are by nature two-dimensional, potentially having a larger impact than dislocations on pinning DWs, which are two-dimensional as well. The pinning of DWs on grain boundaries could indeed be observed directly, *e.g.* with Lorentz TEM in bulk FeCo alloys.[22,76] The reason for pinning at a grain boundary is the various disruptions in the material, such as mismatch of crystalline lattices, strain and possibly accumulation of impurities, including non-magnetic. Accordingly, micromagnetic material parameters may be inhomogeneous, including magnetization, anisotropy and ex-

change stiffness. A one-dimensional model of a DW shall reasonably well describe such situations. This has been the focus of many reports for the search of explanations of coercivity in practical materials, and tackling the Brown paradox.[78] Aharoni considered a step[79] or a linear decrease[80] in magnetic anisotropy. This can be generalized to a step[81] or the local variation[82] of any micromagnetic parameter. In all cases the propagation field scales inversely with magnetization, as the result of the balance of the Zeeman pressure against a magnetization-independent energy profile. This is a general feature in the physics of coercivity, valid also in other situations such as elastic DWs bending between pinning sites.[83,84] The only exception is pinning originating from dipolar anisotropy on roughness, as examined in the first case above, whose energy depends on magnetization and scale with M_s^2.

Coming back to our measurements, pinning on grain boundaries is consistent with the decrease in depinning field [18 ± 4 to 13 ± 4 to $7 \pm 2\,\mathrm{mT}$] with increasing Co content and increasing M_s in the as-deposited NW samples (Fig. 1), which all share similar grain sizes (Fig. 3). Besides, this explanation is compatible with a pinning persisting for the $Co_{20}Ni_{80}$ alloy despite its vanishing microscopic sources of anisotropy, unlike the hypothesis of the effect of polycrystallinity examined previously. Furthermore, if the grain boundary area is smaller than the section of the wire, the pinning effect is probably averaged out over multiple grain boundaries. The reduced depinning field for NWs deposited with $\mathrm{pH} = 1.5$ [$14 \pm 3\,\mathrm{mT}$] matches with the reduced grain size compared to the as-deposited NWs [$18 \pm 4\,\mathrm{mT}$]. This is also consistent with the increase of pinning strength upon annealing (Fig. 3) since annealing leads to more extended grain boundaries and also promotes impurity diffusion to the grain boundaries.[85] Lastly, one may expect pinning to decrease with increasing NW diameter, related to the averaging of energy over the number of grains boundaries across the diameter.

Overview and discussion

To conclude the above analysis of various physical reasons for pinning, pinning on geometrical defects such as roughness is expected to result in a scaling with M_s. This is opposite to the experimental trend, ruling out this source of pinning. Models for pinning on materials' defects all predict a scaling of pinning with $1/M_\mathrm{s}$. However, out of the possible consequences of defects, we can rule out that magnetocrystalline and magnetoelastic anisotropy play a major role, as models for these effects would predict a sharp minimum for

the $Co_{20}Ni_{80}$ composition, again opposite to the experimental observations. The most plausible explanation for pinning lies in the role of grain boundaries, able to affect drastically micromagnetic material parameters locally, for which both experiments and modeling agree with a variation of pinning with $1/M_s$. Still, the granular structure of the material has an impact, partially averaging the effect for smaller grain size, and thereby decreasing the pinning effect. Finally, experimental constraints and variability have been such that the DW type could not be differentiated and that the NW diameter could not be kept fixed, which we acknowledge is not ideal for the understanding of the relevant physics. More experiments would be needed to investigate the impact of these parameters on DW pinning in NWs.

Based on the above conclusion, it may be possible to further reduce the depinning field by increasing M_s, here through a larger Co content, however, the occurrence of the hexagonal close packed Co phase above a composition of $Co_{50}Ni_{50}$ [38] may itself increase pinning due to the increasing magnetocrystalline anisotropy. Besides, note that the $1/M_s$ trend may not apply for current-driven DW motion, for which a higher transfer of angular momentum is required for large magnetization. Initial experiments comparing as-deposited and annealed $90\,\mathrm{nm}$ diameter $Co_{30}Ni_{70}$ NWs revealed an increase in depinning current j_{dep} from $1.2 \times 10^{12}\,\mathrm{A/m^2}$ in as-deposited wires to $2.3 \times 10^{12}\,\mathrm{A/m^2}$ in annealed wires, which matches the trend observed under quasistatic fields. However, it appears that the changes in pinning strength have a much greater impact on j_{dep} than on H_{dep}. Finally, although reducing the grain size appears to be an effective method to reducing pinning strength, it also leads to increased resistance in NWs. Therefore, temperature-assisted depinning shall crucially be taken account in the analysis of experiments, and would also imply a higher power consumption in applications.

Conclusions

We have experimentally investigated DW pinning at room temperature in electrodeposited and rather magnetically soft Co_xNi_{100-x} NWs, with $x = 20$, 30 and 40. Pinning is highest for $x = 20$ and decreases linearly with increasing Co content, scaling roughly with $1/M_s$. This observation is not compatible with pinning governed by surface roughness, which should rather increase in proportion to M_s. Also, this does not support the role of magnetocrystalline anisotropy and magnetostriction, as at room temperature these

are lowest nearly simultaneously for the $Co_{20}Ni_{80}$ concentration. This suggests that pinning is governed by microstructural defects such as grain boundaries, supported by information on grain size and boundaries brought by XRD and TEM, and the increase of pinning for larger grain size D. This suggests a handle to controlling DW pinning in electrodeposited wire by decreasing D through engineering of deposition parameters or conversely increasing D by annealing.

Supporting Information

Figure S1, TEM micrographs of CoNi Nws; Figure S2, evaluation of the NW composition as it depends on the electrolyte composition; Figure S3, EDX spectroscopic line scan of a sample of NWs along the wires' long axis; Figure S4, exemplary magnetic hysteresis loops; Table S1, experimental values of M_s and H_c determined for different samples of CoNi alloy NWs, compared with theoretical M_s values; Figure S5, XRD data complementing those presented in Figure 2a. The Supporting Information is available from the authors or the publisher.

Acknowledgements

The authors acknowledge financial support from the ANR-DFG project C3DS (DFG BA4277/12-1, ANR-18-CE92-0045) and the CNRS-CEA "METSA" French network (FR CNRS 3507). M. S. acknowledges a grant from the Laboratoire d'excellence LANEF in Grenoble (ANR-10-LABX-51-01).

References

(1) Sixtus, K. J.; Tonks, L. Propagation of large Barkhausen discontinuities. *Phys. Rev.* **1931**, *37*, 930–958.

(2) Beach, G. S. D.; Nistor, C.; Knuston, C.; Tsoi, M.; Erskine, J. L. Dynamics of field-driven domain-wall propagation in ferromagnetic nanowires. *Nat. Mater.* **2005**, *4*, 741–744.

(3) Thiaville, A.; Nakatani, Y. In *Spin dynamics in confined magnetic structures III*; Hillebrands, B., Thiav-

ille, A., Eds.; Topics Appl. Physics; Springer: Berlin, 2006; Vol. 101; Chapter Domain-wall dynamics in nanowires and nanostrips, pp 161–205.

(4) Mougin, A.; Cormier, M.; Adam, J.; Metaxas, P.; Ferré, J. Domain wall mobility, stability and Walker breakdown in magnetic nanowires. *Europhys. Lett.* **2007**, *78*, 57007.

(5) Boulle, O.; Malinowski, G.; Kläui, M. Current-induced domain wall motion in nanoscale ferromagnetic elements. *Mater. Sc. Eng. R: Rep.* **2011**, *72*, 159–187.

(6) Grimaldi, E.; Krizakova, V.; Sala, G.; Yasin, F.; Couet, S.; Kar, G. S.; Garello, K.; Gambardella, P. Single-shot dynamics of spin–orbit torque and spin transfer torque switching in three-terminal magnetic tunnel junctions. *Nat. Nanotechnol.* **2020**, *15*, 111–117.

(7) Caretta, L.; Mann, M.; Büttner, F.; Ueda, K.; Pfau, B.; Günther, C. M.; Hessing, P.; Churikova, A.; Klose, C.; Schneider, M. et al. Fast current-driven domain walls and small skyrmions in a compensated ferrimagnet. *Nat. Nanotechnol.* **2018**, *13*, 1154–1160.

(8) Parkin, S. S. P. U.S. patents 6834005, 6898132, 6920062. 2004.

(9) Parkin, S. S. P.; Hayashi, M.; Thomas, L. Magnetic Domain-Wall Racetrack Memory. *Science* **2008**, *320*, 190.

(10) Fert, A.; Reyren, N.; Cros, V. Magnetic skyrmions: advances in physics and potential applications. *Nature Reviews Materials* **2017**, *2*, 17031.

(11) Klaui, M.; Ehrke, H.; Rüdiger, U.; Kasama, T.; Dunin-Borkowski, R. E.; Backes, D.; Heyderman, L. J.; Vaz, C. A. F.; Bland, J. A. C.; Faini, G. et al. Direct observation of domain-wall pinning at nanoscale constrictions. *Appl. Phys. Lett.* **2005**, *87*, 102509.

(12) Bogart, L. K.; Atkinson, D.; O'Shea, K.; McGrouther, D.; McVitie, S. Dependence of domain wall pinning potential landscapes on domain wall chirality and pinning site geometry in planar nanowires. *Phys. Rev. B* **2009**, *79*, 054414.

(13) Ivanov, A. A.; Orlov, V. A. A Comparative Analysis of the Mechanisms of Pinning of a Domain Wall in a Nanowire. *Phys. Sol. State* **2011**, *53*, 2441.

(14) Herzer, G. Grain size dependence of coercivity and permeability in nanocrystalline ferromagnets. *IEEE Trans. Magn.* **1990**, *26*, 1397.

(15) Schöbitz, M.; De Riz, A.; Martin, S.; Bochmann, S.; Thirion, C.; Vogel, J.; Foerster, M.; Aballe, L.; Menteş, T. O.; Locatelli, A. et al. Fast domain walls governed by topology and Œsted fields in cylindrical magnetic nanowires. *Phys. Rev. Lett.* **2019**, *123*, 217201.

(16) Kondorski, E. On the nature of coercive force and irreversible changes in magnetisation. *Phys. Z. Sowjetunion* **1937**, *11*, 597.

(17) Kondorski, E. J. *J. Exp. Theor. Fiz.* **1940**, *10*, 420.

(18) Vogel, A.; Wintz, S.; Gerhardt, T.; Bocklage, L.; Strache, T.; Im, M.-Y.; Fischer, P.; Fassbender, J.; McCord, J.; Meier, G. Field- and current-induced domain-wall motion in permalloy nanowires with magnetic soft spots. *Appl. Phys. Lett.* **2011**, *98*, 202501.

(19) Ivanov, Y. P.; Chuvilin, A.; Lopatin, S.; Kosel, J. Modulated Magnetic Nanowires for Controlling Domain Wall Motion: Toward 3D Magnetic Memories. *Am. Chem. Soc. Nano* **2016**, *10*, 5326.

(20) Mohammed, H.; Vidal, E. V.; Ivanov, Y. P.; Kosel, J. Magnetotransport Measurements of Domain Wall Propagation in Individual Multisegmented Cylindrical Nanowires. *IEEE Transactions on Magnetics* **2016**, *52*, 1–5.

(21) Lindquist, A. K.; Feinberg, J. M.; Harrison, R. J.; Loudon, J. C.; Newell, A. J. Domain wall pinning and dislocations: Investigating magnetite deformed under conditions analogous to nature using transmission electron microscopy. *J. Geophys. Res.* **2015**, *120*, 1415–1430.

(22) Yu, R. H.; Basu, S.; Zhang, Y.; Parvizi-Majidi, A.; Xiao, J. Q. Pinning effect of the grain boundaries on magnetic domain wall in FeCo-based magnetic alloys. *J. Appl. Phys.* **1999**, *85*, 6655–6659.

(23) Ferreira, V. A.; Toscano, D.; Leonel, S. A.; Coura, P. Z.; Dias, R. A.; Sato, F. Transverse domain wall scattering and pinning by magnetic impurities in magnetic nanowires. *J. Appl. Phys.* **2013**, *144*, 013907.

(24) Dean, J.; Bryan, M. T.; Schrefl, T.; Allwood, D. A. Stress-based control of magnetic nanowire domain walls in artificial multiferroic systems. *J. Appl. Phys.* **2011**, *109*, 023915.

(25) Lei, N.; Devolder, T.; Agnus, G.; Aubert, P.; Daniel, L.; Kim, J.-V.; Zhao, W.; Trypiniotis, T.; Cowburn, R. P.; Chappert, C. et al. Strain-controlled magnetic domain wall propagation in hybrid piezoelectric/ferromagnetic structures. *Nat. Commun.* **2013**, *4*, 1378.

(26) Bochmann, S.; Fernandez-Pacheco, A.; Mačkovič, M.; Neff, A.; Siefermann, K. R.; Spiecker, E.; Cowburn, R. P.; Bachmann, J. Systematic tuning of segmented magnetic nanowires into three-dimensional arrays of 'bits'. *RCS Adv.* **2017**, *7*, 37627.

(27) Metlov, K. L.; Guslienko, K. Y. Stability of magnetic vortex in soft magnetic nano-sized circular cylinder. *J. Magn. Magn. Mater.* **2002**, *242*, 1015.

(28) Fernandez-Pacheco, A.; Streubel, R.; Fruchart, O.; Hertel, R.; Fischer, P.; Cowburn, R. P. Three-dimensional magnetism. *Nat. Commun.* **2017**, *8*, 15756.

(29) Wieser, R.; Vedmedenko, E. Y.; Weinberger, P.; Wiesendanger, R. Current-driven domain wall motion in cylindrical nanowires. *Phys. Rev. B* **2010**, *82*, 144430.

(30) Yan, M.; Andreas, C.; Kakay, A.; Garcia-Sanchez, F.; Hertel, R. Fast domain wall dynamics in magnetic nanotubes: Suppression of Walker breakdown and Cherenkov-like spin wave emission. *Appl. Phys. Lett.* **2011**, *99*, 122505.

(31) Hertel, R. Ultrafast domain wall dynamics in magnetic nanotubes and nanowires. *J. Phys.: Condens. Matter* **2016**, *28*, 483002.

(32) Hayashi, M.; Thomas, L.; Bazaliy, Y. B.; Rettner, C.; Moriya, R.; Jiang, X.; Parkin, S. S. P. Influence of Current on Field-Driven Domain Wall Motion in Permalloy Nanowires from Time Resolved Measurements of Anisotropic Magnetoresistance. *Phys. Rev. Lett.* **2006**, *96*, 197207.

(33) Sellmyer, D. J.; Zheng, M.; Skomski, R. Magnetism of Fe, Co and Ni nanowires in self-assembled arrays. *J. Phys.: Condens. Matter* **2001**, *13*.

(34) Nielsch, K.; Hertel, R.; Wehrspohn, R. B.; Barthel, J.; Kirschner, J.; Gösele, U.; Fischer, S. F.; Kronmüller, H. Switching Behavior of Single Nanowires Inside Dense Nickel Nanowire Arrays. *IEEE Trans. Magn.* **2002**, *38*, 2571.

(35) Hertel, R.; Kirschner, J. Magnetization reversal dynamics in nickel nanowires. *Physica B* **2004**, *343*, 206.

(36) Qin, J.; Nogués, J.; Mikhaylova, M.; Roig, A.; noz, J. S. M.; Muhammed, M. Differences in the magnetic properties of Co, Fe, and Ni 250-300 nm wide nanowires electrodeposited in amorphous anodized alumina templates. *Chem. Mater.* **2005**, *17*, 1829–1834.

(37) Pitzschel, K.; Bachmann, J.; Martens, S.; Montero-Moreno, J. M.; Kimling, J.; Meier, G.; Escrig, J.; Nielsch, K.; Görlitz, D. Magnetic reversal of cylindrical nickel nanowires with modulated diameters. *J. Appl. Phys.* **2011**, *109*, 033907.

(38) Vivas, L. G.; Vazquez, M.; Escrig, J.; Allende, S.; Altbir, D.; Leitao, D. C.; Araujo, J. P. Magnetic anisotropy in CoNi nanowire arrays: Analytical calculations and experiments. *Phys. Rev. B* **2012**, *85*.

(39) Ivanov, Y. P.; Vázquez, M.; Chubykalo-Fesenko, O. Magnetic reversal modes in cylindrical nanowires. *J. Phys. D: Appl. Phys.* **2013**, *46*, 485001.

(40) Pereira, A.; Gallardo, C.; Espejo, A. P.; Briones, J.; Vivas, L. G.; Vázquez, M.; Denardin, J. C.; Escrig, J. Tailoring the magnetic properties of ordered 50-nm-diameter CoNi nanowire arrays. *Journal of Nanoparticle Research* **2013**, *15*.

(41) Bochmann, S.; Döhler, D.; Trapp, B.; Staňo, M.; Wartelle, A.; Fruchart, O.; Bachmann, J. Preparation and physical properties of soft magnetic nickel-cobalt nanowires with modulated diameters. *J. Appl. Phys.* **2018**, *124*, 163907.

(42) Dolocan, V. O. Domain wall pinning and interaction in rough cylindrical nanowires. *Appl. Phys. Lett.* **2014**, *105*, 162401.

(43) Berganza, E.; Bran, C.; Vazquez, M.; Asenjo, A. Domain wall pinning in FeCoCu bamboo-like nanowires. *Sci. Rep.* **2016**, *6*, 29702.

(44) Nasirpouri, F.; Peighambari-Sattari, S.-M.; Palmero, C. B. E. M.; Eguiarte, E. B.; Vazquez, M.; Patsopoulos, A.; Kechrakos, D. Geometrically designed domain wall trap in tri-segmented nickel magnetic nanowires for spintronics devices. *Sci. Rep.* **2019**, *9*, 1–11.

(45) Fernandez-Roldan, J. A.; Riz, A. D.; Trapp, B.; Thirion, C.; Toussaint, J. C.; Fruchart, O.; Gusakova, D. Modeling of the magnetic-field-induced domain wall propagation in modulated diameter cylindrical nanowires. *Sci. Rep.* **2019**, *9*, 5130.

(46) Riz, A. D.; Trapp, B.; Fernandez-Roldan, J.; Thirion, C.; Toussaint, J.-C.; Fruchart, O.; Gusakova, D. *Magnetic Nano- and Microwires*; Elsevier, 2020; Chapter Domain wall pinning in a circular cross-section wire with modulated diameter, pp 427–453.

(47) Bran, C.; Berganza, E.; Fernandez-Roldan, J. A.; Palmero, E. M.; Meier, J.; Calle, E.; Jaafar, M.; Foerster, M.; Aballe, L.; Rodriguez, A. F. et al. Magnetization Ratchet in Cylindrical Nanowires. *Am. Chem. Soc. Nano* **2018**, *12*, 5932–5939.

(48) Franchin, M.; Knittel, A.; Albert, M.; Chernyshenko, D.; Fischbacher, T.; Prabhakar, A.; Fangohr, H. Enhanced spin transfer torque effect for transverse domain walls in cylindrical nanowires. *Phys. Rev. B* **2011**, *84*, 094409.

(49) Kadowaki, S.; Takahashi, M. Magnetostriction constants of Nickel-Cobalt alloys. *J. Phys. Soc. Jap.* **1981**, *50*, 1154.

(50) Natter, H.; Hempelmann, R. Nanocrystalline copper by pulsed electrodeposition: The effects of organic additives, bath temperature, and pH. *J. Phys. Chem.* **1996**, *100*, 19525–19532.

(51) Alper, M.; Kockar, H.; Safak, M.; Baykul, M. C. Comparison of NiCu alloy films electrodeposited at low and high pH levels. *J. Alloys. Compd.* **2008**, *453*, 15–19.

(52) Qin, D.; Wang, C.; Sun, Q.; Li, H. The effects of annealing on the structure and magnetic properties of CoNi patterned nanowire arrays. *Appl. Phys. A* **2002**, *74*, 761–765.

(53) Tóth, B. G.; Péter, L.; Révész, A.; Pádár, J.; Bakonyi, I. Temperature dependence of the electrical

resistivity and the anisotropic magnetoresistance (AMR) of electrodeposited Ni-Co alloys. *Eur. Phys. J. B* **2010**, *75*, 167–177.

(54) Wang, Y. M.; Cheng, S.; Wei, Q. M.; Ma, E.; Nieh, T. G.; Hamza, A. Effects of annealing and impurities on tensile properties of electrodeposited nanocrystalline Ni. *Scripta Mater.* **2004**, *51*, 1023–1028.

(55) Staňo, M.; Fruchart, O. In *Handbook of Magnetic Materials*; Brück, E., Ed.; Elsevier, 2018; Vol. 27; Chapter Magnetic nanowires and nanotubes.

(56) Jamet, S.; Rougemaille, N.; Toussaint, J. C.; Fruchart, O. In *Magnetic Nano- and Microwires: Design, synthesis, properties and applications*; Vazquez, M., Ed.; Woodhead, 2015; Chapter Head-to-head domain walls in one-dimensional nanostructures: an extended phase diagram ranging from strips to cylindrical wires, pp 783–811.

(57) Biziere, N.; Gatel, C.; Lassalle-Balier, R.; Clochard, M. C.; Wegrowe, J. E.; Snoeck, E. Imaging the Fine Structure of a Magnetic Domain Wall in a Ni Nanocylinder. *Nano Lett.* **2013**, *13*, 2053.

(58) Da Col, S.; Jamet, S.; Rougemaille, N.; Locatelli, A.; Menteş, T. O.; Burgos, B. S.; Afid, R.; Darques, M.; Cagnon, L.; Toussaint, J. C. et al. Observation of Bloch-point domain walls in cylindrical magnetic nanowires. *Phys. Rev. B* **2014**, *89*, 180405.

(59) Wartelle, A.; Trapp, B.; Staňo, M.; Thirion, C.; Bochmann, S.; Bachmann, J.; Foerster, M.; Aballe, L.; Menteş, T. O.; Locatelli, A. et al. Bloch-point-mediated topological transformations of magnetic domain walls in cylindrical nanowires. *Phys. Rev. B* **2019**, *99*, 024433, arXiv:1806.10918.

(60) Williamson, G. K.; Hall, W. H. X-ray line broadening from filed aluminium and wolfram. *Acta Metall. Mater.* **1953**, *1*, 22–31.

(61) Mote, V. D.; Purushotham, Y.; Dole, B. N. Williamson-Hall analysis in estimation of lattice strain in nanometer-sized ZnO particles. *J. Theor. Appl. Phys.* **2012**, *6*, 2–8.

(62) Riemer, S.; Gong, J.; Sun, M.; Tabakovic, I. Influence of Solution pH and Concentration of Saccharin on Electrodeposition and Properties of 2.4 T CoFe Alloys. *J. Electrochem. Soc.* **2009**, *156*, D439–D447.

(63) Rashidi, A. M.; Amadeh, A. The effect of current density on the grain size of electrodeposited nanocrystalline nickel coatings. *Surf. Coat. Technol.* **2008**, *202*, 3772–3776.

(64) Rashidi, A. M.; Amadeh, A. The effect of saccharin addition and bath temperature on the grain size of nanocrystalline nickel coatings. *Surf. Coat. Technol.* **2009**, *204*, 353–358.

(65) Ebrahimi, F.; Bourne, G. R.; Kelly, M. S.; Matthews, T. E. Mechanical properties of nanocrystalline nickel produced by electrodeposition. *Nanostr. Mater.* **1999**, *11*, 343–350.

(66) Kang, J.-X.; Zhao, W.-Z.; Zhang, G.-F. Influence of electrodeposition parameters on the deposition rate and microhardness of nanocrystalline Ni coatings. *Surf. Coat. Technol.* **2009**, *203*, 1815–1818.

(67) Mishra, R.; Basu, B.; Balasubramaniam, R. Effect of grain size on the tribological behavior of nanocrystalline nickel. *Materials Science and Engineering: A* **2004**, *373*, 370–373.

(68) Park, D.-Y.; Song, R. Y.; Ko, J. M.; Yoo, B. Y.; Myung, N. V. Stress Changes of Nanocrystalline CoNi Thin Films Electrodeposited from Chloride Baths. *Electrochem. Solid-State Lett.* **2005**, *8*, C23.

(69) Dost, R.; Zhou, Y.; Zhang, H.; Allwood, D. A.; Inkson, B. J. Effect of annealing on the electrical and magnetic properties of electrodeposited Ni and permalloy nanowires. *J. Magn. Magn. Mater.* **2020**, *499*, 166276.

(70) Becker, R.; Döring, W. *Ferromagnetismus*; Springer, 1939.

(71) Bruno, P. Dipolar magnetic surface anisotropy in ferromagnetic thin films with interfacial roughness. *J. Appl. Phys.* **1988**, *64*, 3153–3156.

(72) Lee, W.; Kim, J.-C.; Gösele, U. Spontaneous Current Oscillations during Hard Anodization of Aluminum under Potentiostatic Conditions. *Adv. Funct. Mater.* **2010**, *20*, 21–27.

(73) Cornelius, T. W.; Schiedt, B.; Severin, D.; Pépy, G.; Toulemonde, M.; Apel, P. Y.; Boesecke, P.; Trautmann, C. Nanopores in track-etched polymer membranes characterized by small-angle x-ray scattering. *Nanotechnology* **2010**, *21*, 155702.

(74) Herzer, G. Nanocrystalline soft magnetic materials. *J. Magn. Magn. Mater.* **1992**, *112*, 258–262.

(75) Kadowaki, S.; Takahashi, M. Magnetocrystalline Anisotropy of Nickel-Cobalt Alloys. *J. Phys. Soc. Jap.* **1975**, *38*, 1612–1619.

(76) Yu, R. H.; Basu, S.; Ren, L.; Zhang, Y.; Parvizi-Majidi, A.; Unruh, K. M.; Xiao, J. Q. High temperature soft magnetic materials: FeCo alloys and composites. *IEEE Trans. Magn.* **2000**, *36*, 3388–3393.

(77) Abraham, C.; Aharoni, A. Simple Model for Nucleation around Dislocations. *Phys. Rev.* **1962**, *128*, 2496–2499.

(78) Brown, W. F. *Micromagnetics*; Wiley, 1963.

(79) Aharoni, A. Reduction in Coercive Force Caused by a Certain Type of Imperfection. *Phys. Rev.* **1960**, *119*, 127–131.

(80) Abraham, C.; Aharoni, A. Linear Decrease in the Magnetocrystalline Anisotropy. *Phys. Rev.* **1960**, *120*, 1576–1579.

(81) Hagedorn, F. B. Analysis of exchange-coupled magnetic thin films. *J. Appl. Phys.* **1970**, *41*, 2491.

(82) Leineweber, T.; Kronmüller, H. Micromagnetic examination of exchange coupled ferromagnetic nanolayers. *J. Magn. Magn. Mater.* **1997**, *176*, 145–154.

(83) Döring, W. Über das Anwachsen der Ummagnetisierungskeime bei großen Barkhausen-Sprüngen. *Z. Phys.* **1938**, *108*, 137–152.

(84) Kersten, M. Zur Theorie der Koerzitivkraft. *Zeitschrift für Physik* **1948**, *124*, 714–741.

(85) Wang, Z. K.; Kuok, M. H.; Ng, S. C.; Lockwood, D. J.; Cottam, M. G.; Nielsch, K.; Wehrspohn, R. B.; Gösele, U. Spin-Wave Quantization in Ferromagnetic Nickel Nanowires. *Phys. Rev. Lett.* **2002**, *89*.

TOC Graphic